



# An Experimental Study on the Dependency of Thermal Resistance of Additively Manufactured Micro-Channel Heat Sinks on Channel Cross-Sections

A.N. Kivanani<sup>1</sup> · S. Khalilpourazary<sup>1</sup> · F. Mobadersani<sup>1</sup>

Received: 3 September 2023 / Accepted: 5 February 2024 / Published online: 21 February 2024  
© The Society for Experimental Mechanics, Inc 2024

## Abstract

Cooling by micro-channel heat sink transfers excess heat flux in electrical devices and increases their functional capacity, reliability, and life span. In this paper, AISi10Mg powders were employed to create four micro-channel heat sinks with cross-sections including square, rectangle, circle, and ellipse with an additive manufacturing method. To investigate the impact of micro-channel heat sink cross-sectional geometry on thermal resistance, Taguchi's L25 orthogonal array was utilized. Reynolds number and electric power were selected to be the input parameters. The experimental tests were conducted using an experimental setup and distilled water as the working fluid in the laminar flow regime. The results obtained from the experimental tests indicated that in the range of electric power from 4 to 12 W and Reynolds numbers of 50, 100, 150, 200, and 250, the micro-channel heat sink with a square cross-section exhibits the highest heat transfer performance. Finally, an analysis of variance was conducted to study the impact of the Reynolds number and electric power factors on thermal resistance. The findings revealed the significant effect of electric power on thermal resistance in micro-channel heat sinks compared to the Reynolds number in the laminar regime. Additionally, a comparison was made with other available results.

**Keywords** Micro-channel heat sink · Channel cross-section · Selective laser melting · Thermal resistance · Electric power

## Introduction

Equipment miniaturization and a tendency to enhance efficiency have led to increased heat in electronic systems. This phenomenon has turned the importance of the cooling system into a big challenge. As the heat flux generated in an electronic system increases, its functional capacity, reliability, and life are extremely affected. Researches demonstrate that the performance reliability in electronic systems depends on their temperature for example in temperatures range of 70 °C to 80 °C, an increase of 1 °C decreases the system's performance reliability by 5% [1]. To overcome this challenge, aluminum and copper Micro-Channel Heat Sinks (MCHSs) with a working fluid such as water can be employed to dissipate away the heat generated in the system. There is a series of micro-scale grooves with various

cross-sections such as rectangles, circles, etc. in MCHSs as a path for the working fluid to pass through [2].

Conventional machining processes such as micromachining, microsawing [3], and laser micromachining [4] are used for machining simple geometries in MCHSs. During the process of machining, chips are produced as waste materials. Nevertheless, developing the Computer-Aided Design (CAD) technique has greatly helped designers to make complex geometries to achieve optimum thermal performance in MCHSs. Additive Manufacturing (AM) is a process that has currently been taken into account by MCHS manufacturers [5]. In this process, the three-dimensional physical model of the part is fabricated by placing layers with a two-dimensional cross-section and a certain thickness. Accordingly, cavities and thin wall structures (TWSs) can be constructed with high accuracy, layer by layer, using a bottom-up method [6]. Moreover, despite the conventional manufacturing methods such as micromachining, the high ability of AM technology is capable of fabricating complex geometries of fins and flow paths in micro and millimeter scales.

Many studies have simulated/investigated the effect of different types of channel cross-sections on the heat

✉ S. Khalilpourazary  
s.khalilpour@mee.uut.ac.ir

<sup>1</sup> Department of Mechanical Engineering, Urmia University of Technology, Urmia, Iran

performance of MCHSs, but each method for MCHS production creates its fingerprint. For example, the internal surfaces of the micro-channels have different roughnesses or tolerances based on the production methods. This fact can directly affect the thermal performance of MCHSs by changing laminar flow into turbulent flow and vice versa.

Mohammed et al., numerically simulated the effect of using Nano aluminum oxide in the Reynolds range of 100 to 1000 in laminar flow [7]. The goal was to study the thermal resistance and the characteristics of fluid flow in a MCHS with a rectangular cross-section. The results showed that using Nano aluminum oxide fluid resulted in a better heat transfer compared to using water. Moreover, in high heat flux conditions, the thermal resistance of MCHSs decreases by increasing the volume fraction of nanoparticles. Hung et al. numerically analyzed the heat transfer characteristics of a double-layer MCHS [8]. The effect of the number of channels, width-to-pitch ratio, channel aspect ratio, wall thickness, pumping power in fluid distribution, pressure drop, and heat resistance with different coolant fluids, such as glycerol, ethylene glycol, and distilled water, were assumed as variable parameters. The results presented that in similar conditions, the thermal performance of the double-layer MCHS was on average 6.3% better than that of the single-layer MCHS. Also, it was shown that increasing pumping power and using distilled water improved the heat transfer performance of MCHSs. Fani et al. simulated the changes in total thermal resistance in a MCHS with a trapezoidal cross-section in laminar flow [9]. The size and the volume fraction of copper oxide particles in the working fluid were selected as the input parameters. The results confirmed that thermal resistance increased as the temperature and volume fraction increased and the size of the particles decreased. Alfaryjat et al. studied silicon MCHSs with rhombus, hexagonal, and circular cross-sections in the Reynolds number range of 100 to 1000 [10]. The results obtained from the simulation included studying the effects of channel geometry on thermal resistance and pressure drop. The results also proved that MCHSs with rhombus, hexagonal, and circular cross-sections have the minimum thermal resistance, respectively. Halelfadl et al. simulated the thermal performance of MCHSs with rectangular cross-section in laminar flow using carbon nanotubes water-based nanofluids [11]. The volume fraction percentage of nanoparticles was chosen in the range of 0.0055% to 0.55% and then the effect of volume fraction on thermal resistance was investigated. The results confirmed that using carbon nanotubes would lead to higher cooling compared to using water. It was also shown that the thermal resistance was the lowest in 0.01% volume fraction percentage. Ayatollahi et al. using the Finite Volume Method (FVM) simulated heat transfer in MCHSs in laminar flow [12]. Distilled water was chosen as the working fluid in analyses and the performances of a simple single-layer heat sink,

a heat sink with an adjustable horizontal separator plate, and a double-layer heat sink with truncated upper channels were simulated. The input parameters included wall thickness, the thickness of the separation plate, the number of micro-channels, the vertical position of the separation plate, the velocity ratio, and the length ratio. The results substantiated that the double-layer heat sink with truncated upper channels had the lowest thermal resistance as the output parameter. Collins et al. applied the Additive Manufacturing (AM) technology to generate straight and manifold micro-channels made of AlSi10Mg material and with hydraulic diameters of 500 $\mu\text{m}$  [13]. Water was employed as the working fluid and the thermal performance in the mass flux range of 500 kg/m<sup>2</sup>s to 2000 kg/m<sup>2</sup>s was investigated. The results showed that in laminar flow the hydraulic performance of the straight micro-channel was predictable. It was also shown that the complicated design of the manifold micro-channel decreased the pressure drop. Xu et al. scrutinized the thermal performance of a three-layered MCHS manufactured by the Selective Laser Melting (SLM) method with four types of pulsating flows: driven by square, triangular, saw tooth, and sinusoidal wave signals [14]. Graphene-oxide-platelets (GOPs, 0.4 wt%)-water nanofluid was utilized as the working fluid. The results showed that the steady flow at the same pump power is bigger than that of the average pulsating flow rate. Also, increasing the pump power enhances not only the thermal performance of the manufactured heat sink but also the heat transfer enhancement factor  $\eta$  of the pulsating flow. Ozguc et al. employed the interior-point method to simulate Permeable Membrane Micro-Channel (PMM) heat sink and Straight Micro-Channel (SMC) heat sink to achieve minimum heat resistance and pressure drop [15]. Then, the optimum heat sinks were manufactured from AlSi10Mg powders using AM technology. The results indicated that with a specific pressure drop in PMM heat sink, thermal resistance decreased by 68% compared to SMC heat sink.

Tan et al. studied the shape and geometry changes of micro-channels on their capability to cool the electronic chips [16]. By carrying out numerical simulation, heat sinks with straight micro-channels and spider-netted micro-channels were selected to manufacture using AM technology. Experimental tests proved the high heat transfer of spider-netted heat sinks compared to that of straight MCHSs. Moreover, the results proved the effect of geometry on the thermal performance of manufactured MCHSs.

Ozguc et al. employed topology optimization algorithms to manufacture heat sinks with high thermal performance [17]. The design of pin fin microstructures with different grid cell sizes and fin thicknesses was selected to fabricate the MCHSs with the AM technology. To achieve the minimum pressure drop and minimum thermal resistance, the grid cell size and the parameters of the AM technology were chosen as the input parameters in the designed functions. The results of

optimization algorithms were employed to optimize the micro-channel's topography. The comparison of experiments with model predictions for pressure drop and thermal resistance parameters shows the high precision of the proposed method. Kong et al. designed a compact Manifold Micro-Channel Heat Sink (MMCHS) and employed numerical simulation to analyze the flow [18]. Then the thermal performance results of simulation and experiments using single-phase water cooling were compared. The results showed that MMCHS dissipated the effective heat flux up to  $240 \text{ W/cm}^2$  with a mass flow rate of  $395 \text{ g/min}$  with a low-pressure drop of  $1.7 \text{ kPa}$  and a low heated surface temperature of  $100 \text{ }^\circ\text{C}$ . Moreover, the experiments showed that the  $100$  to  $200 \text{ g/min}$  flow rate causes a  $24\%$  drop in thermal resistance.

Based on the literature review and considering the various methods for producing MCHSs and the special effects of each manufacturing method on the appearance and dimensional characteristics of MCHSs, trusting the simulated results can cause mistakes in the thermal performance evaluation of the MCHSs. So, this paper aims to help scientists comprehend the impact of the manufacturing method and micro-channel geometries on the fabricated MCHSs. To cover this significant research gap, four different micro-channel geometries with square, circular, oval, and rectangular cross-sections were manufactured by AM technology and compared with similar samples simulated in previous investigations. AlSi10Mg was employed as raw material to fabricate MCHSs with the SLM method. Then by considering electric power and Reynolds number as the input parameters, the effect of the geometry of cross-sections in MCHSs on thermal resistance was investigated. Also, Analysis of Variance (ANOVA) was employed to assess the significance of Reynolds number and electric power on the thermal resistance of all types of MCHSs. Finally, a comparison had been performed with other available results.

Collins et al. showed that the high surface roughness in the internal surfaces of the micro-channels led to a transition to turbulent flow [13]. Ozguc et al. presented that changes in surface roughness of SMC and PMM heat sinks due to different pore sizes and porosity of internal surfaces directly affect their thermal performance and create a transition to turbulent flow [15]. Narendran et al. investigated the thermal performance of two MCHSs produced by micro-Wire Electric Discharge Machining ( $\mu$ -WEDM) and 3D printing methods [19]. The material of both heat sinks was chosen from Ti64. The results showed that the high surface roughness of the internal surfaces in MCHSs changes the heat transfer and thermal enhancement factor leading to a transition to turbulent flow. Presented studies have proved that the effect of internal surfaces on the

thermal performance of MCHSs is significant just in turbulent flow regimes [20, 21]. This paper explores the thermal resistance of MCHSs in experimental tests with controlled input parameters. The tests were conducted under laminar flow conditions and Reynolds numbers less than  $2000$ . Therefore, the effect of surface roughness on the results of the tests was practically ignored.

## Materials and Methods

### Material and Manufacturing Method

AlSi10Mg is an aluminum alloy with high mechanical and thermal properties. AlSi10Mg powder is vastly employed in AM to manufacture heat sinks [22, 23]. In the present study, the AlSi10Mg powder has a spherical shape with an average diameter of  $20 \mu\text{m}$ , and its chemical composition is presented in Table 1. Previous researches declare that the thermal conductivity coefficient of AlSi10Mg alloy can be increased up to  $180 \frac{\text{W}}{\text{m}\cdot\text{K}}$  in AM technology [24].

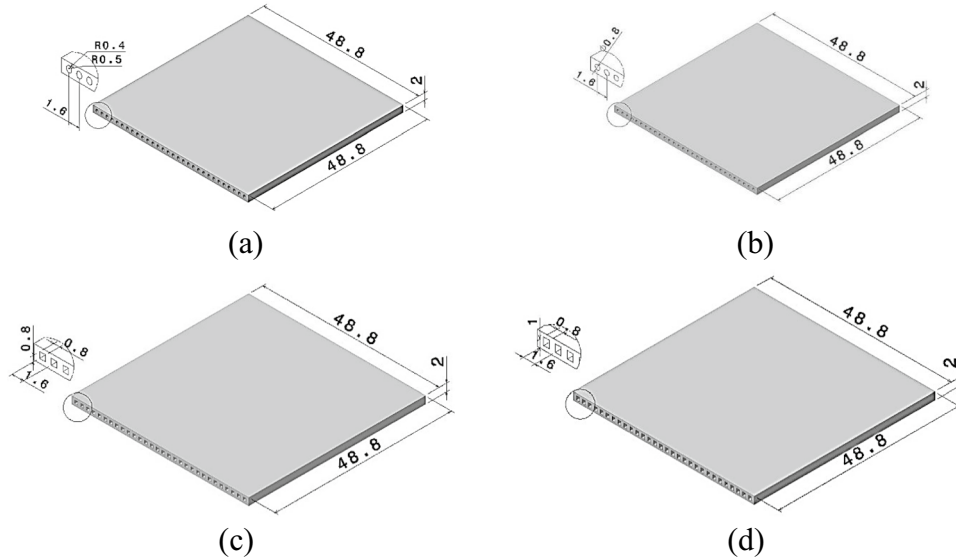
The SLM method was employed in this research to manufacture MCHSs in Noura M100P machine with a fiber laser of  $300 \text{ W}$  power. First, a recoater arm spreads the metal powder such as AlSi10Mg with a specific thickness on the build platform, and with a high power ytterbium fiber laser beam moving in a certain path the metal powders are sintered and attached. Then, the platform moves downward and the displacement of the platform is determined by the thickness of the next layer. By repeating the process the three-dimensional object is fabricated in a bottom-up method. In this research, the build chamber was filled with nitrogen gas to protect the part against oxidation. The thickness of each layer while manufacturing the samples was determined to be  $30 \mu\text{m}$ . The dimensions of MCHSs with square, rectangle, circle, and ellipse cross-sections manufactured through the SLM method are presented in Fig. 1. In all of the samples, the number of channels and pitch value among them are  $30$ , and  $1.6 \text{ mm}$ , respectively. After AM process, to reduce the porosity and to remove fluid leakage in manufactured MCHSs, heat treatment process was performed at  $300 \text{ }^\circ\text{C}$  for  $2 \text{ h}$ .

### Experimental Setup

The orientation of the experimental setup for the flow loop system used to carry out experimental tests is shown in Fig. 2.

**Table 1** Chemical composition of the used AlSi10Mg powders

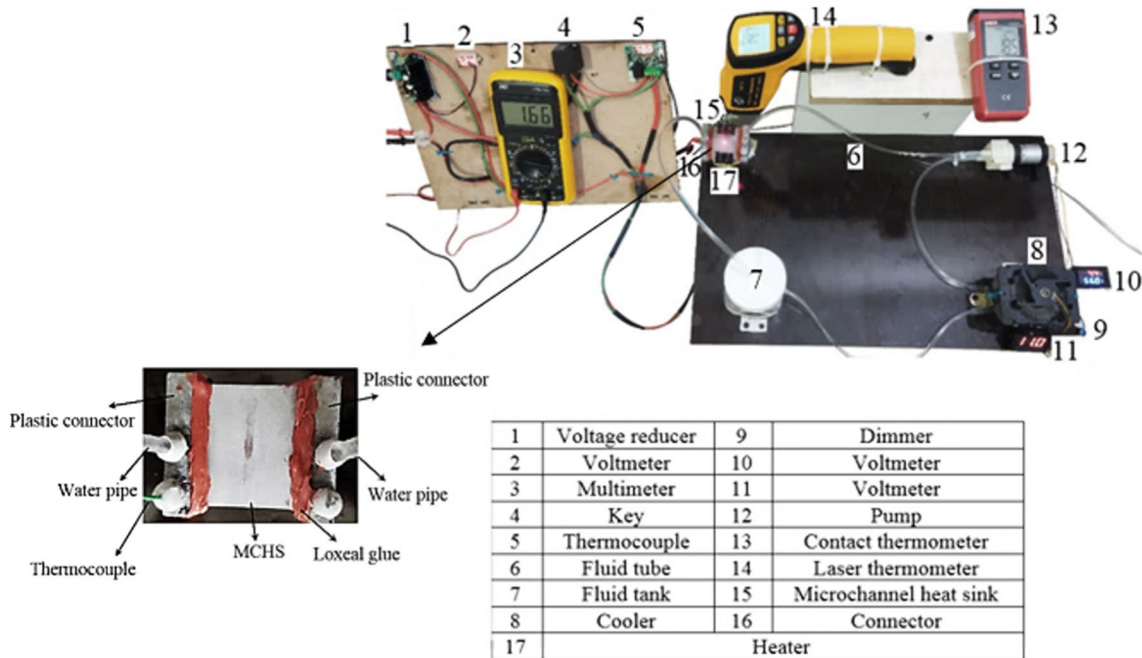
Element	Al	Si	Fe	Cu	Mn	Mg	Ni	Zn	Pb	Sn
Weight %	balanced	9	0.39	0.05	0.35	0.43	0.05	0.1	0.05	0.05



**Fig. 1** Dimensions of the designed MCHSs for the SLM process: (a) ellipse, (b) circle, (c) square, and (d) rectangle (in millimeters)

In this research, a contact thermometer of model UNI-T UT320A (No.13 in Fig. 2) was used to measure the average temperature of the micro-channel bottom surface, and a digital multimeter of model EXCEL DT-9205A (No.3 in Fig. 2) was employed to measure the electric current. Moreover, two voltmeters were utilized to evaluate the electric power and Reynolds number during experimental tests. A voltmeter of model DSN-VC288 (No.2 in Fig. 2) was used to measure the electric

power and a voltage reducer (No.1 in Fig. 2) was employed to control it. The electric power values are measured by the multimeter (No.3 in Fig. 2). The voltmeter (No.11 in Fig. 2) is used to control the pumping power of the pump (No.12 in Fig. 2) with the help of a dimmer of the SA-608 model (No.9 in Fig. 2). In other words, the values of the voltage given to the pump are changed by the dimmer and due to that the pumping power of the fluid can be increased or decreased. Thus, the



**Fig. 2** Experimental setup of flow loop facility

Reynolds number was controlled by a dimmer and this voltmeter throughout the experiment. The chosen values for the Reynolds number in this research were 50, 100, 150, 200, and 250. The voltmeter (No.10 in Fig. 2) is attached to a cooling system with a fan which shows the changes in the temperature of the input working fluid in MCHSs via the changes in the voltage. The value of the voltage shown in this voltmeter and at stable condition indicates that the temperature of the input fluid during the tests is fixed at 15.6 °C. The working fluid used in the experiments is distilled water. The diaphragm pump (No.12 in Fig. 2) works under maximum voltage of 12 V and has a maximum volumetric flow rate of 15  $\frac{m^3}{s}$ . To apply heat flux to the MCHS during the tests, a heater (No.17 in Fig. 2), which was insulated under the MCHSs by glass wool, was employed. The temperature of the heater was controlled by a thermocouple (No.5 in Fig. 2). During the experiments, the average temperature of the heater surface for the input powers of 4, 6, 8, 10, and 12 W were 30, 40, 50, 60, and 70 °C, respectively. The supply power voltage and current for the fluid flow loop system were 12 V and 20A, respectively. Two plastic connectors were employed to allow distilled water to enter and exit the channels of the MCHSs. The inlet and outlet pipes

were connected to each connector and sealed with silicone glue. The thermocouple wire was also embedded in one of the connectors and sealed using silicone glue. The Loxeal glue (with thermal conductivity of 0.1 W/m<sup>2</sup>.K) made of liquid Teflon was employed to connect both connectors to each side of MCHS. Loxeal glue is highly resistant to heat to 150 °C and humidity. Then, the heater was placed under the MCHS and sealed with the bottom surface of the MCHS by using silicone paste. The silicone paste acted as a heat conductor, transferring the whole generated heat of the heater to the MCHS. To insulate the heater from the surrounding environment, glass wool, which is a heat insulator, was also used. Figure 3 shows a schematic diagram of the experimental setup which includes a pump, MCHS, heater, water tank, voltmeters, dimmer, power supply, thermocouple, and pipelines.

Adjusting the input temperature of the fluid is the most important factor in measuring the Reynolds number. For all the MCHSs at the beginning of each test in a condition that the electric circuit system of Fig. 2 is disabled, the input temperature of the fluid is fixed at 15.6 °C in stable condition. Under this condition, the values shown by the voltmeter (No.10 in Fig. 2) and the contact thermometer (No.13 in Fig. 2) do not

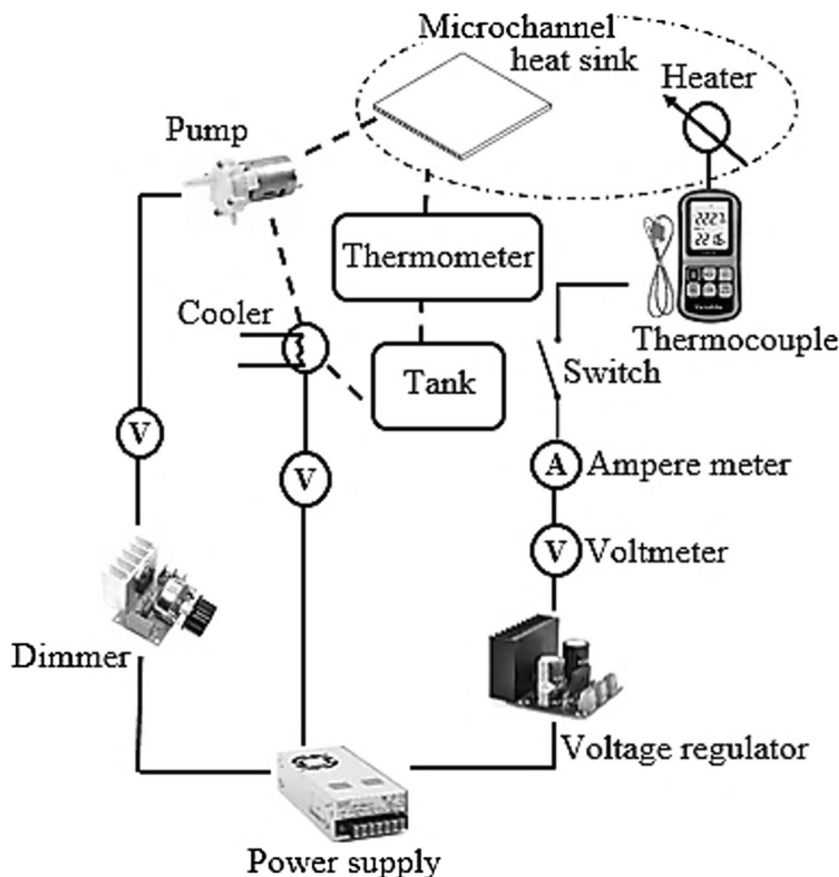


Fig. 3 Schematic diagram of the experimental flow loop facility, black lines represent the electrical line, and dotted lines represent fluid pipelines



change, even as time goes by. In the second phase, the density and viscosity of the fluid were assessed using equations (1), (2), and (3) at 15.6 °C [25].

$$\rho = 1000 - 0.0178(T - 4)^{1.7} \quad (1)$$

$$\ln \frac{\mu}{\mu_0} = -1.704 - 5.306\aleph - 7.003\aleph^2 \quad (2)$$

$$\aleph = \frac{273}{273 + T} \quad (3)$$

where,  $\rho$  is the density ( $\frac{\text{Kg}}{\text{m}^3}$ ) at temperature  $T$  (°C),  $\aleph$  is the temperature ratio based on fluid temperature,  $\mu$  is the viscosity at temperature  $T$  (°C), and  $\mu_0$  is the viscosity of the fluid at 0°C which is  $1.788 \times 10^{-3}$  Pa.s [25]. The density and viscosity of the working fluid in the present study were determined as  $998.85 \frac{\text{Kg}}{\text{m}^3}$  and  $0.00113$  Pa.s, respectively. After that and by applying different voltage rates to the pump, the mass of the output fluid was measured for one minute so that the Reynolds number for each voltage and mass could be obtained via equations (4) to (7) [25, 26].

$$V = \frac{M}{\rho} \quad (4)$$

$$Q = \frac{V}{t} \quad (5)$$

$$U = \frac{Q}{nA} \quad (6)$$

$$\text{Re} = \frac{\rho UD}{\mu} \quad (7)$$

where,  $V$  is the volume ( $\text{m}^3$ ),  $M$  is mass (Kg),  $t$  is time (s),  $Q$  is the volumetric flow rate ( $\text{m}^3/\text{s}$ ),  $U$  is flow velocity (m/s),  $\text{Re}$  is the Reynolds number,  $n$  is the number of channels (30 channels), and  $A$  is the cross-section area of each channel ( $\text{m}^2$ ). Since the purpose of applying the equations mentioned above was to obtain the mass of the output fluid of the pump to achieve Reynolds numbers of 50, 100, 150, 200, and 250, the values of the fluid mass for each Reynolds number were obtained from equations (4) to (7) are presented in Table 2.

**Table 2** Fluid mass values for each Reynolds number

No.	Reynolds numbers	Mass (gr)
1	50	64
2	100	128
3	150	192
4	200	256
5	250	320

**Table 3** Selected factors and assigned levels in this study

Parameters	Level				
	1	2	3	4	5
Electric power (W)	4	6	8	10	12
Reynolds numbers	50	100	150	200	250

According to Table 3 in this study, the input parameters of electric power and Reynolds number were considered in 5 levels to analyze the output parameter of thermal resistance. Taguchi's L25 orthogonal array was utilized to design the experiments. These experiments were similarly repeated for each MCHSs with square, rectangle, circle, and ellipse cross-section. The designed experiments are depicted in Table 4.

## Results and Discussion

Figure 4 shows the manufactured MCHSs by the SLM method. The cross-section images of the MCHSs were prepared using a Canon EOS Rebel T6i camera with a 45 mm lens through macro photography.

**Table 4** Experimental test conditions on Taguchi L25

No.	Electric power (W)	Reynolds numbers
1	4	50
2	4	100
3	4	150
4	4	200
5	4	250
6	6	50
7	6	100
8	6	150
9	6	200
10	6	250
11	8	50
12	8	100
13	8	150
14	8	200
15	8	250
16	10	50
17	10	100
18	10	150
19	10	200
20	10	250
21	12	50
22	12	100
23	12	150
24	12	200
25	12	250

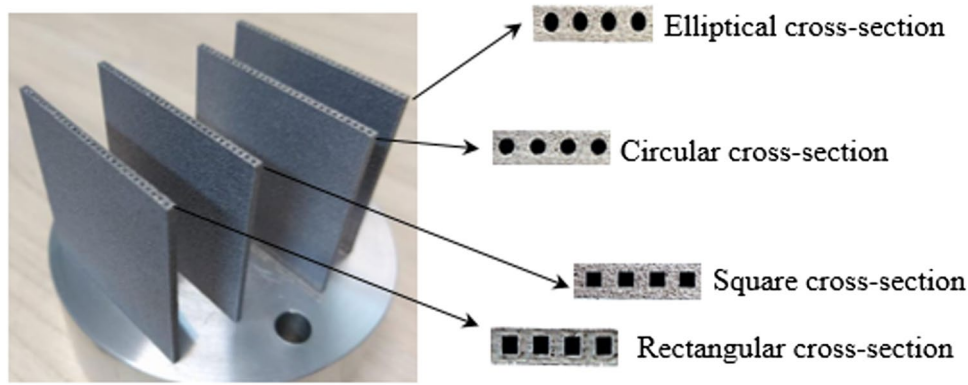


Fig. 4 MCHSs manufactured by the SLM method

Thermal resistance, as a factor dependent on temperature and electric power, has a direct effect on heat transfer in designing and manufacturing MCHSs. Lower thermal resistances refers to higher heat transfer from the hot surface. Hence, thermal resistance plays a key role in determining the performance efficiency of MCHSs in electronic systems. The thermal resistance value can be obtained from equation (8) [27].

$$R_{th} = \frac{T_b - T_{in}}{V_{eff} I_{eff}} \quad (8)$$

where,  $T_b$ ,  $T_{in}$ ,  $V_{eff}$ ,  $I_{eff}$ ,  $R_{th}$ , are average temperature of the micro-channel bottom surface ( $^{\circ}K$ ), inlet average temperature ( $^{\circ}K$ ), effective voltage (V), effective current (A), which are introduced in equation (18), and thermal resistance ( $\frac{K}{W}$ ), respectively. The MCHS bottom temperature ( $T_b$ ) can be obtained by the following analytical equation:

$$T_b = T_H - \left( \frac{t_s}{k_s} + \frac{t_f}{k_f} \right) q \quad (9)$$

In which  $T_H$  is the upper surface temperature of the MCHS which measured by the laser thermometer (No.14 in Fig. 2),  $q$  is the heat flux and  $(t_s, k_s)$  and  $(t_f, k_f)$  are the thickness and thermal conductivity of the MCHSs material and water, respectively.

### Uncertainty Analysis

In this study, all thermocouples are calibrated against a reference thermometer and the maximum measurement errors of the thermocouples are 1.5%. The measurement uncertainties for the ammeter and the voltmeter are 1.8% and 1% of full scale, respectively. All the analysis presented in this section is based on the methodology proposed by

Coleman and Steele [28]. Equation (10) was used to determine uncertainty [28].

$$u(R) = \sqrt{\sum c_i^2 u_i^2} \quad (10)$$

Here,  $c_i$  is the partial derivative of thermal resistance based on voltage, electric current, and temperature parameters, and  $u_i$  is also the measurement error of each related equipment. Equations (11) to (14) indicate the method to obtain the thermal resistance uncertainty in this study.

$$c_T = \frac{\partial R}{\partial T} = \frac{1}{VI} \quad (11)$$

$$c_I = \frac{\partial R}{\partial I} = \frac{-T}{VI^2} \quad (12)$$

$$c_V = \frac{\partial R}{\partial V} = \frac{-T}{V^2 I} \quad (13)$$

$$\begin{aligned} u(R) &= \sqrt{\sum c_i^2 u_i^2} = \sqrt{\left(\frac{1}{VI}\right)^2 u_T^2 + \left(\frac{-T}{VI^2}\right)^2 u_I^2 + \left(\frac{-T}{V^2 I}\right)^2 u_V^2} \\ &= R \times \sqrt{\frac{u_T^2}{T^2} + \frac{u_I^2}{I^2} + \frac{u_V^2}{V^2}} \end{aligned} \quad (14)$$

Table 5 presents the thermal resistance uncertainties for each of the MCHSs with square, rectangle, circle, and ellipse cross-sections. The values of thermal resistance uncertainties for MCHSs are presented in the form of error bar in Fig. 5. Figure 5, based on Taguchi’s L25 orthogonal array, shows the effects of electric power in Reynolds numbers 50, 100, 150, 250, and 250 on the thermal resistance for all the cross-sections of MCHSs.

Table 6 shows the numerical values of thermal resistance in Fig. 5 for each MCHS based on Taguchi’s L25 orthogonal array.

**Table 5** Calculated thermal resistance uncertainties for manufactured MCHSs

No.	Reynolds	Electric power (W)	Uncertainty			
			Rectangle	Square	Circle	Ellipse
1	50	4	$1.9 \times 10^{-3}$	$0.4 \times 10^{-3}$	$0.4 \times 10^{-3}$	$2.4 \times 10^{-3}$
2	50	6	$2.9 \times 10^{-3}$	$0.4 \times 10^{-3}$	$0.7 \times 10^{-3}$	$2.5 \times 10^{-3}$
3	50	8	$3.1 \times 10^{-3}$	$0.5 \times 10^{-3}$	$1.5 \times 10^{-3}$	$2.6 \times 10^{-3}$
4	50	10	$3.4 \times 10^{-3}$	$0.8 \times 10^{-3}$	$1.6 \times 10^{-3}$	$3.5 \times 10^{-3}$
5	50	12	$3 \times 10^{-3}$	$1.2 \times 10^{-3}$	$1.5 \times 10^{-3}$	$2.1 \times 10^{-3}$
6	100	4	$2.4 \times 10^{-3}$	$0.4 \times 10^{-3}$	$0.9 \times 10^{-3}$	$2.7 \times 10^{-3}$
7	100	6	$2.9 \times 10^{-3}$	$0.4 \times 10^{-3}$	$1.3 \times 10^{-3}$	$2.8 \times 10^{-3}$
8	100	8	$3.2 \times 10^{-3}$	$0.5 \times 10^{-3}$	$1.7 \times 10^{-3}$	$2.6 \times 10^{-3}$
9	100	10	$3.6 \times 10^{-3}$	$0.9 \times 10^{-3}$	$1.6 \times 10^{-3}$	$2.4 \times 10^{-3}$
10	100	12	$3.3 \times 10^{-3}$	$1.1 \times 10^{-3}$	$1.6 \times 10^{-3}$	$2.5 \times 10^{-3}$
11	150	4	$3 \times 10^{-3}$	$0.4 \times 10^{-3}$	$0.4 \times 10^{-3}$	$3.9 \times 10^{-3}$
12	150	6	$2.9 \times 10^{-3}$	$0.4 \times 10^{-3}$	$1.3 \times 10^{-3}$	$1.6 \times 10^{-3}$
13	150	8	$3.4 \times 10^{-3}$	$0.6 \times 10^{-3}$	$1.9 \times 10^{-3}$	$1.7 \times 10^{-3}$
14	150	10	$3.9 \times 10^{-3}$	$1.1 \times 10^{-3}$	$1.7 \times 10^{-3}$	$2.2 \times 10^{-3}$
15	150	12	$3.3 \times 10^{-3}$	$1.2 \times 10^{-3}$	$1.8 \times 10^{-3}$	$2.5 \times 10^{-3}$
16	200	4	$3 \times 10^{-3}$	$0.4 \times 10^{-3}$	$0.9 \times 10^{-3}$	$4.4 \times 10^{-3}$
17	200	6	$3.5 \times 10^{-3}$	$0.4 \times 10^{-3}$	$1.3 \times 10^{-3}$	$1.6 \times 10^{-3}$
18	200	8	$3.8 \times 10^{-3}$	$0.6 \times 10^{-3}$	$1.9 \times 10^{-3}$	$2.4 \times 10^{-3}$
19	200	10	$4 \times 10^{-3}$	$1.2 \times 10^{-3}$	$1.2 \times 10^{-3}$	$2.8 \times 10^{-3}$
20	200	12	$3.4 \times 10^{-3}$	$1.4 \times 10^{-3}$	$1.7 \times 10^{-3}$	$2.6 \times 10^{-3}$
21	250	4	$4.5 \times 10^{-3}$	$0.4 \times 10^{-3}$	$0.9 \times 10^{-3}$	$3.5 \times 10^{-3}$
22	250	6	$5.3 \times 10^{-3}$	$0.5 \times 10^{-3}$	$1.6 \times 10^{-3}$	$2.7 \times 10^{-3}$
23	250	8	$4.3 \times 10^{-3}$	$0.8 \times 10^{-3}$	$2 \times 10^{-3}$	$2.7 \times 10^{-3}$
24	250	10	$3.8 \times 10^{-3}$	$1.3 \times 10^{-3}$	$1.8 \times 10^{-3}$	$2.8 \times 10^{-3}$
25	250	12	$3.5 \times 10^{-3}$	$1.4 \times 10^{-3}$	$1.8 \times 10^{-3}$	$2.6 \times 10^{-3}$

COMSOL Multiphysics v6.2 was employed to evaluate the velocity and pressure field in each MCHS geometry configuration. Figure 6 demonstrates the pressure distribution inside one micro-channel. For the numerical simulations, the inlet velocity was set based on the inlet Reynolds number ( $Re = 250$ ), the no-slip boundary condition at the walls, and also the zero-pressure outlet boundary condition was assumed. It was observed that the pressure distribution decreased from the inlet to the outlet in all configurations. Moreover, the maximum essential inlet pressures for different cross-sections are illustrated. The results reveal that the maximum pressure drop among the geometries belongs to the circular cross-section, and oppositely minimum pressure drop for the rectangular cross-section is evaluated. Using this parameter can aid in designing the MCHS with the minimum pumping power. It is worth noting that the pressure drop of each MCHS can be derived by modeling a single micro-channel due to the equality of the pressure drop in parallel channels.

Overall pressure drop for different cross-section geometries and also Reynolds numbers are presented in Table 7. The results demonstrate that by increasing the inlet Reynolds number, the pressure drop for all geometries augments.

This is verified by the experimental results and also the fundamental hydraulic laws (Darcy-Weisbach equation). The simulation results indicate that when using circular cross-section MCHS, there is a higher pressure drop, leading to increased pumping power for all Reynolds numbers. On the other hand, utilizing a rectangular cross-section is recommended for MCHS due to the minimum pressure drop.

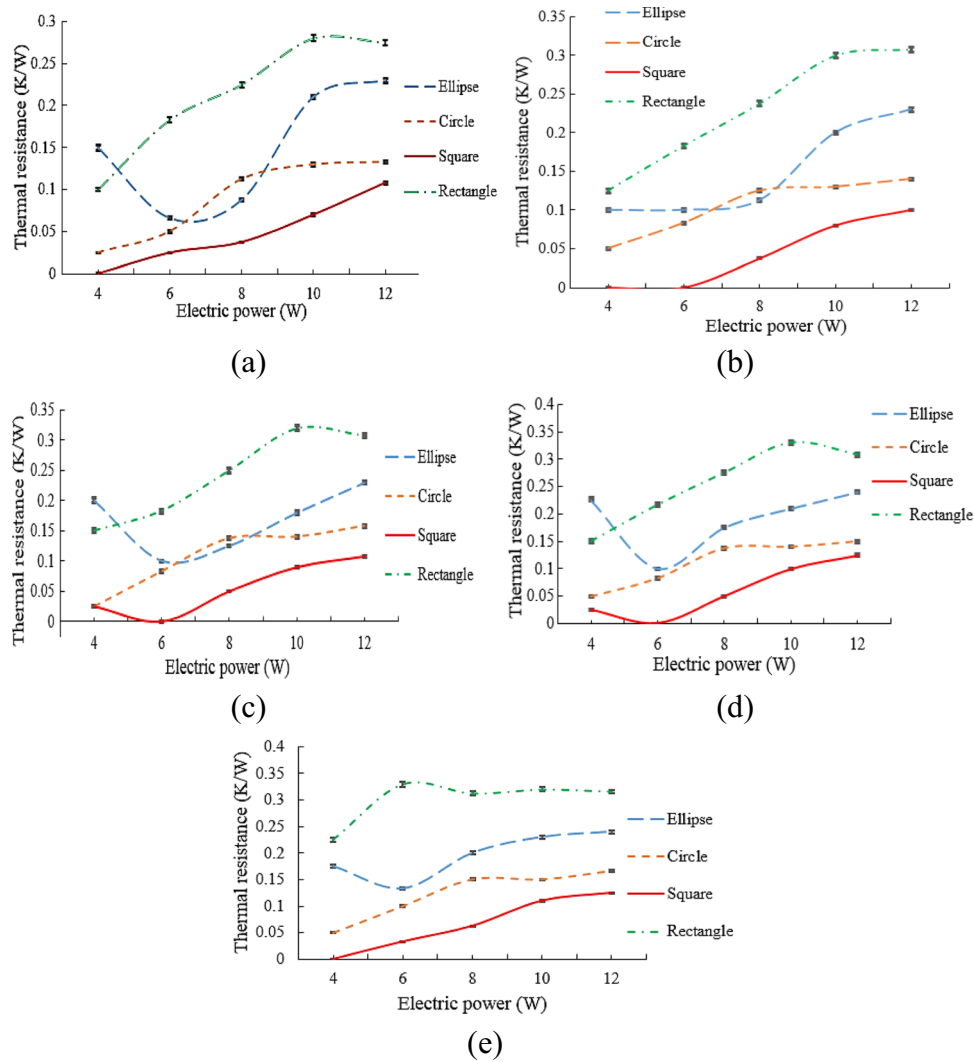
Hydraulic diameter is a term commonly used to handle the flow in non-circular tubes and channels. According to the square, rectangle, and ellipse cross-sections, the hydraulic diameter for uniform cross-section along the channel length can be obtained by equation (15) [29].

$$D_H = \frac{4S}{P} \quad (15)$$

where  $D_H$ ,  $S$ , and  $P$  are the hydraulic diameter, the cross-sectional area of the flow, and the wetted perimeter of the cross-section, respectively. In this study, the hydraulic diameters of square and circle were  $800 \mu\text{m}$ , and  $880 \mu\text{m}$  for rectangle and ellipse. Table 8 depicts the flow rate values for each MCHS with different cross-sectional shapes.

Previous studies showed that as the hydraulic diameter of the channel cross-section decreased, the thermal resistance

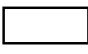

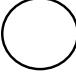





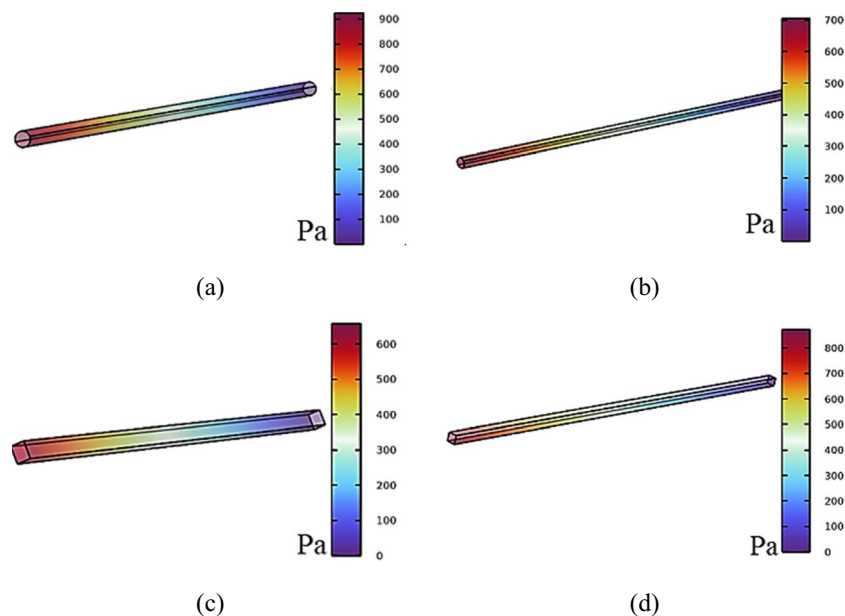
**Fig. 5** Comparison of the thermal resistance in MCHSs with ellipse, circular, rectangle, and square cross-sections in Reynolds number: (a) 50, (b) 100, (c) 150, (d) 200, and (e) 250

of the heat sink decreased and the heat transfer increased [30, 31]. Thus, the increase in the thermal resistance of the rectangular micro-channel in Fig. 5 can be due to its hydraulic diameter. As reported by Mohammed et al. [32] and Abouali and Baghernezhad [33], as the hydraulic diameter increases, the thermal resistance increases. On the other hand, due to the creation of dead flow at the vicinity of the walls in MCHSs with a rectangular cross-section, rectangular cross-sections have a higher thermal resistance. Because as the hydraulic diameter increases, the area of the dead flow regions augments. As a result, the thickness of the thermal boundary layer will have a higher development rate, which leads to a decrease in the heat transfer rate from the hot surface. Mohammed et al. simulated the thermal boundary layer in the rectangular channels [32]. The results show that the rectangular channels have a thicker thermal boundary layer

alongside the flow that causes heat transfer to decrease by increasing the thickness of the boundary layer. So, the fact that a rectangle cross-section has a higher thermal resistance compared to an ellipse cross-section can be related to the higher thickness of its thermal boundary layer. Abouali and Baghernezhad proved that arc-shaped cross-sections had a more optimal heat transfer performance compared to cross-sections with straight edges [33]. The results attained from this study justified the lower thermal resistance and higher heat transfer of circle and ellipse cross-sections compared to a rectangular cross-section. Employing computer simulation, Alfaryjat et al. showed that a rhombus cross-section had a lower thermal resistance compared to circular and hexagonal cross-sections [10]. As the rhombus cross-section is very similar to the square cross-section employed in this study, the fall in the thermal resistance of the square cross-section

No.	Reynolds number	Electric power (W)	Thermal resistance ( $\frac{K}{W}$ )			
						
1	50	4	0.1	0.0004	0.025	0.175
2	50	6	0.183	0.025	0.05	0.21
3	50	8	0.225	0.0375	0.1125	0.24
4	50	10	0.28	0.07	0.13	0.175
5	50	12	0.275	0.108	0.133	0.23
6	100	4	0.125	0.0004	0.05	0.1
7	100	6	0.183	0.0004	0.083	0.1
8	100	8	0.2375	0.0375	0.125	0.1125
9	100	10	0.3	0.08	0.13	0.2
10	100	12	0.308	0.1	0.14	0.23
11	150	4	0.15	0.025	0.025	0.2
12	150	6	0.183	0.0004	0.083	0.1
13	150	8	0.25	0.05	0.1375	0.175
14	150	10	0.32	0.09	0.14	0.21
15	150	12	0.308	0.108	0.158	0.24
16	200	4	0.15	0.025	0.05	0.225
17	200	6	0.2166	0.0004	0.083	0.1
18	200	8	0.275	0.05	0.1375	0.175
19	200	10	0.33	0.01	0.14	0.21
20	200	12	0.308	0.125	0.15	0.24
21	250	4	0.225	0.0004	0.05	0.175
22	250	6	0.33	0.033	0.1	0.133
23	250	8	0.3125	0.0625	0.15	0.2
24	250	10	0.32	0.11	0.15	0.23
25	250	12	0.316	0.125	0.166	0.24

**Table 6** Experimental results for the thermal resistance of each MCHS



**Fig. 6** Pressure drop simulations considering  $Re=250$  for different cross section geometries: (a) circle, (b) ellipse, (c) rectangle, and (d) square

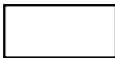

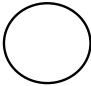

**Table 7** Simulated results for the pressure drop of each MCHS

Reynolds numbers	Pressure drop (Pa)			
	Rectangle	Square	Circle	Ellipse
50	102.28	136.67	152.98	114.94
100	214.81	287.40	318.74	240.05
150	339.53	454.65	500.14	377.58
200	476.75	638.29	697.56	527.88
250	626.19	837.53	911.53	690.98

compared to the circular cross-section in Fig. 5 can be justified. However, some cross-sections have a different thermal resistance from the general trend of diagrams in certain electric powers. Equation (8) shows that thermal resistance is affected by the difference between the average temperature of the micro-channel bottom surface, inlet average temperature, and the electric power changes. As the electric power increases, the heat flux increases which leads to an increase in the average temperature of the micro-channel bottom surface. Thus, the temperature difference in equation (8) increases and directly causes an increase in thermal resistance. For instance, in Reynolds numbers 50, 150, and

200 the differences between the  $T_m$ ,  $T_{in}$  temperatures of the fluid at an electric power of 4 W are 0.6 °C and 0.4 °C for ellipse and rectangle cross-sections, respectively. Thus, the increase in the temperature difference at this electric power has led to a temporary increase in the thermal resistance in the ellipse cross-section. The other exceptions in Fig. 5 were because of this very same reason. According to Fig. 5, it can be concluded that in Reynolds numbers between 50 and 250, MCHSs with square and rectangle cross-sections have the lowest and highest thermal resistance, respectively. Moreover, Fig. 5 depicts that the thermal resistance of some MCHS configurations decreases with an increase in electric power. Due to the higher uncertainty for the thermal resistance calculation of specific geometry of MCHS (i.e., Elliptic or circular) in lower fluid flow rates and heat fluxes, the thermal resistance results against the bottom heat flux demonstrate fluctuations reported by previous studies [18]. It is worth mentioning, that the authors repeated the corresponding experiments according to the calculation of the thermal resistance of elliptic and circular geometries, and the same results were achieved with acceptable tolerances.

The comparison between the thermal resistance range for the MCHSs with different cross-sections in this study

MCHS cross-section geometry	Reynolds numbers	Flow rate (mm <sup>3</sup> /s)	MCHS cross-section geometry	Reynolds numbers	Flow rate (mm <sup>3</sup> /s)
	50	34.540		50	34.540
	100	69.080		100	69.080
	150	103.620		150	103.620
	200	138.160		200	138.160
	250	172.700		250	172.700
	50	31.400		50	31.400
	100	62.800		100	62.800
	150	94.200		150	94.200
	200	125.600		200	125.600
	250	157.000		250	157.000

**Table 8** The flow rate of each MCHS in this study at different Reynolds number

**Table 9** Comparison between the thermal resistances obtained from the present study with previous studies

No.	Researchers	Year	MCHS geometry	Thermal resistance	Present research
1	Wang et al. [34]	2011	Rectangle	0.1-0.35	0.1-0.33
2	Hung et al. [8]	2012	Two-layer Rectangle	0.12-0.26	0.1-0.33
3	Lin et al. [35]	2014	Two-layer Rectangle	0.16-0.36	0.1-0.33
4	Alfaryjat et al. [10]	2014	Circle	0.06-0.21	0.025-0.166
5	Leng et al. [36]	2016	Rectangle	0.18-0.48	0.1-0.33
6	Wang et al. [31]	2016	Rectangle	0.1-0.25	0.1-0.33
7	Ayatollahi et al. [12]	2021	Simple single-layer	0.14-0.22	0.1-0.33
8	Ozguç et al. [15]	2021	Rectangle	0.12-0.3	0.1-0.33

and the results of the computer simulations from previous studies is presented in Table 9. The results show that the thermal resistance of circle and rectangle cross-sections is very similar to that of previous studies. Table 9 prove the high capability of the thermal performance of AlSi10Mg in fabricating MCHSs with the SLM process. Because there has been no study on MCHSs with square and ellipse cross-sections, no comparison is presented in Table 9.

### Specifying the Heat Loss in MCHSs

Despite using different techniques to create thermal insulation in experimental tests, the heat losses have been investigated in this section. If the MCHS contains a static fluid, due to the small size of the micro-channels, the only mechanism of heat transfer will be conduction, and the effects of natural displacement can be ignored [37]. By using the following analytical relationship, the spatial distribution of micro-channel surface temperature can be obtained at different times [37]:

$$T_{an}(H, t) = T_i + \frac{2q\sqrt{\alpha t}}{k} \left[ \frac{\exp\left(-\frac{H}{2\sqrt{\alpha t}}\right)}{\sqrt{\pi}} - \frac{H}{2\sqrt{\alpha t}} \operatorname{erfc}\left(\frac{H}{2\sqrt{\alpha t}}\right) \right] \quad (16)$$

where,  $H$ ,  $T_{an}$ ,  $T_i$ , and  $\alpha$  are height of micro-channel, analytical solution of temperature distribution of MCHS setup, initial temperature of MCHS plus water setup, and equivalent temperature diffusion of AlSi10Mg and water, respectively. On the other hand, considering that the average temperature of the surface of the micro-channel ( $T_H$ ) is measured using a laser thermocouple for specified times, it is possible to calculate the heat loss rate through the temperature difference created between  $T_H$  and  $T_{an}$ . By performing various tests based on the applied heat fluxes, the following linear relationship has the least squared error to fit the heat loss rate results:

$$Q_{loss} = 0.0172(T_{an} - T_H)(q - 4) + 0.2141 \quad (17)$$

In this way, the effective power applied to the micro-heater can be shown as follows:

$$Q_{eff} = (V.I)_{eff} = (V.I)_{app} - Q_{loss} \quad (18)$$

In which “eff” and “app” refer to effective and applied electrical power, respectively. As demonstrated in equations (17) and (18), the heat losses from the setup occur by the natural convection into the surroundings. The value of this term was calculated by specifying the surface temperature of the MCHS according to the presented equations. Equation (18) illustrates the relation of the heat losses as a function of the electric power, proving that the maximum heat losses

**Table 10** Analysis of variance for the MCHS with elliptical cross-section

Source	DF	Adj SS	Adj MS	F-Value	P Value
Electric power (W)	4	0.056100	0.014025	19.35	0.001
Reynolds	4	0.009901	0.002475	3.42	0.034
Error	16	0.011596	0.000725		
Total	24	0.077597			

**Table 11** Analysis of variance for the MCHS with circular cross-section

Source	DF	Adj SS	Adj MS	F-Value	P Value
Electric power (W)	4	0.043250	0.010813	174.65	0.001
Reynolds	4	0.002868	0.000717	11.58	0.001
Error	16	0.000991	0.000062		
Total	24	0.047109			

**Table 12** Analysis of variance for the MCHS with a square cross-section

Source	DF	Adj SS	Adj MS	F-Value	P Value
Electric Power (W)	4	0.042669	0.010667	82.90	0.001
Reynolds	4	0.001625	0.000406	3.16	0.043
Error	16	0.002059	0.000129		
Total	24	0.046353			

**Table 13** Analysis of variance for the MCHS with rectangular cross-section

Source	DF	Adj SS	Adj MS	F-Value	P Value
Electric Power (W)	4	0.094361	0.023590	76.55	0.001
Reynolds	4	0.013461	0.003365	10.92	0.001
Error	16	0.004931	0.000308		
Total	24	0.112752			

from the setup are about 6% for maximum input electric power. So, one can find the related upper performance bound of the performance by the following steps: calculating the heat losses according to the specific input electric power using equation (17) or adding the calculated heat losses in the previous step into the results presented in the results section.

### Analysis of the Thermal Resistance Results

ANOVA is a suitable method to analyze the significance of Reynolds number and electric power factors on thermal

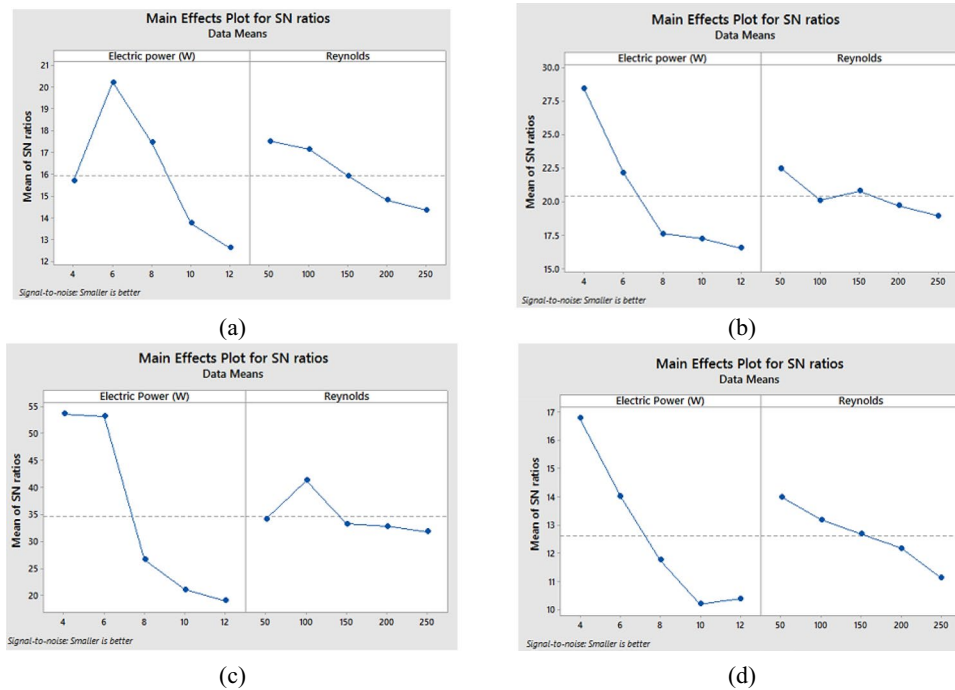


Fig. 7 Response graphs for the S/N ratio of the MCHS: (a) ellipse, (b) circular, (c) square, and (d) rectangular

resistance. Based on the concepts of ANOVA and by choosing the confidence level of 95%, the P values lower than 0.05 and higher than 0.05 identify the effective and ineffective factors, respectively. Effective parameters cause remarkable changes in the results of the experiments [38]. Tables 10, 11, 12 and 13 depict the P values for the MCHSs with square, rectangle, circle, and ellipse cross-sections. The results indicate the significant effect of input parameters on thermal resistance. Also, in all the Tables the F-value for electric power is higher than that of the Reynolds number which indicates that the changes in electric power have a more remarkable impact on thermal resistance in all the MCHSs than the Reynolds number. The S/N ratio response graphs of electric power and Reynolds number on thermal resistance for MCHSs with square, rectangle, circle, and ellipse cross-sections are presented in Fig. 7. Scrutinizing the graphs shows that the total mean of the S/N ratio of the electric power, which is obtained from the average of the values on the vertical axis, is higher than the total mean of the S/N ratio of the Reynolds number. Thus, it can be concluded that the electric power parameter is the dominant parameter of thermal resistance. Findings show that in the diagram of Fig. 7(a) the electric power of 6 W (level 2 in Table 3) and the Reynolds of 50 (level 1 in Table 3) ellipse cross-section has the lowest thermal resistance. Additionally, it can be seen in Figs. 6(b) and 7(d) that the circle and rectangle cross-sections in the Reynolds of 50 (level 1 in Table 3) and the electric power of 4 W (level 1 in Table 3)

and square cross-section in the Reynolds of 100 (level 2 in Table 3) and the electric power of 4 W (level 1 in Table 3) have the lowest thermal resistance.

### Concluding Remarks

In this research, MCHSs with square, rectangle, circle, and ellipse cross-sections were manufactured using the SLM method. In the design of the experiments using the Taguchi method Reynolds number and electric power were selected as the input parameters and thermal resistance was considered as the output parameter. Then, Taguchi’s L25 orthogonal array was employed to study the effect of the channel cross-section of the manufactured MCHSs on thermal resistance. Measuring thermal resistance for experimental levels was carried out using an experimental setup. In addition, ANOVA was utilized to study the impact of Reynolds number and electric power on thermal resistance. Based on the results the following conclusions can be made:

1. The experimental tests show that the MCHS with a square cross-section has the lowest thermal resistance and the highest heat transfer. The results reveal that the thermal resistance of the MCHSs increases in the circle, ellipse, and rectangle cross-sections, respectively.
2. Thermal resistance range in all electric powers and Reynolds numbers investigated in this paper for cir-



cular, rectangular, square, and ellipse cross-sections are  $0.025\text{--}0.166\frac{\text{K}}{\text{W}}$ ,  $0.1\text{--}0.33\frac{\text{K}}{\text{W}}$ ,  $0.0004\text{--}0.125\frac{\text{K}}{\text{W}}$ , and  $0.1\text{--}0.24\frac{\text{K}}{\text{W}}$ , respectively.

3. MCHS with a square cross-section has the highest thermal resistance at an electric power of 12 W for Reynolds numbers 200 and 250, equivalent to  $0.125\frac{\text{K}}{\text{W}}$ .
4. The highest thermal resistance value for the rectangular cross-section of MCHS is  $0.33\frac{\text{K}}{\text{W}}$  at Reynolds numbers 200 and 250 for electric powers 10 and 6 W.
5. MCHS with a circular cross-section has the highest thermal resistance at an electric power of 12 W for Reynolds number 250, equivalent to  $0.166\frac{\text{K}}{\text{W}}$ .
6. The highest thermal resistance for the elliptical cross-section is  $0.24\frac{\text{K}}{\text{W}}$ , which is obtained in Reynolds numbers 150, 200, and 250 for 12 W electric power.
7. The simulation results show that the circular cross-section has the highest pressure drop while the rectangular cross-section has the lowest.
8. Comparing the results from the present study and previous research studies, most of which were performed based on computer simulation (Table 9), shows that the SLM process is an adequate method to manufacture MCHSs.
9. Comparing the thermal resistance of the MCHSs manufactured in this study with the simulation results in Table 9 indicates the proper thermal performance of AlSi10Mg in fabricating MCHSs.
10. The results from ANOVA show that the electric power in all MCHSs has a higher effect on thermal resistance comparing the Reynolds number.

## Declarations

**Conflict of Interest** The authors declare that there is no conflict of interest.

## References

1. Sarvar-Ardeh S, Rafee R, Rashidi S (2023) A comparative study on the effects of channel divergence and convergence on the performance of two-layer microchannels. *Exp Tech* 47:109–122. <https://doi.org/10.1007/s40799-022-00546-9>
2. Ghasemiasl R, Hashemi S, Armaghani T, Tayebi T, Pour MS (2023) Recent studies on the forced convection of nano-fluids in channels and tubes: a comprehensive review. *Exp Tech* 47:47–81. <https://doi.org/10.1007/s40799-022-00558-5>
3. Li X, Fu D, Xu W, Yuan D, Jiang X, Fu T, Chu X, Gao Y, Zhou W (2022) Fabrication of high aspect ratio ceramic micro-channel in diamond wire sawing as catalyst support used in micro-reactor for hydrogen production. *Int J Hydrog Energy* 47:35123–35135. <https://doi.org/10.1016/j.ijhydene.2022.08.103>
4. Faisal N, Zindani D, Kumar K, Bhowmik S (2019) Laser micromachining of engineering materials—a review. *Micro and nano machining of engineering materials: recent developments*. Springer, Cham. [https://doi.org/10.1007/978-3-319-99900-5\\_6](https://doi.org/10.1007/978-3-319-99900-5_6)
5. Nafis BM, Whitt R, Iradukunda AC, Huitink D (2021) Additive manufacturing for enhancing thermal dissipation in heat sink implementation: a review. *Heat Transfer Eng* 42:967–984. <https://doi.org/10.1080/01457632.2020.1766246>
6. Khorasani M, Leary M, Downing D, Rogers J, Ghasemi A, Gibson I, Brudler S, Rolfe B, Brandt M, Bateman S (2023) Numerical and experimental investigations on manufacturability of Al–Si–10Mg thin wall structures made by LB-PBF. *Thin-Walled Struct* 188:110814. <https://doi.org/10.1016/j.tws.2023.110814>
7. Mohammed HA, Gunnasegaran P, Shuaib NH (2010) Heat transfer in rectangular microchannels heat sink using nanofluids. *Int. Commun. Heat and Mass Transfer*. 37:1496–1503. <https://doi.org/10.1016/j.icheatmasstransfer.2010.08.020>
8. Hung TC, Yan WM, Li WP (2012) Analysis of heat transfer characteristics of double-layered microchannel heat sink. *Int Commun Heat and Mass Transfer* 55:3090–3099. <https://doi.org/10.1016/j.ijheatmasstransfer.2012.02.038>
9. Fani B, Kalteh M, Abbassi A (2015) Investigating the effect of Brownian motion and viscous dissipation on the nanofluid heat transfer in a trapezoidal microchannel heat sink. *Adv Powder Technol* 26:83–90. <https://doi.org/10.1016/j.appt.2014.08.009>
10. Alfaryjat AA, Mohammed HA, Adam NM, Ariffin MKA, Najafabadi MI (2014) Influence of geometrical parameters of hexagonal, circular, and rhombus microchannel heat sinks on the thermohydraulic characteristics. *Int. Commun. Heat and Mass Transfer*. 52:121–131. <https://doi.org/10.1016/j.icheatmasstransfer.2014.01.015>
11. Halefadi S, Adham AM, Mohd-Ghazali N, Maré T, Estellé P, Ahmad R (2014) Optimization of thermal performances and pressure drop of rectangular microchannel heat sink using aqueous carbon nanotubes based nanofluid. *Appl. Thermal Eng.* 62:492–499. <https://doi.org/10.1016/j.applthermaleng.2013.08.005>
12. Ayatollahi SM, Ahmadpour A, Hajmohammadi MR (2022) Performance evaluation and optimization of flattened microchannel heat sinks for the electronic cooling application. *J Thermal Analysis and Calorimetry* 147:3267–3281. <https://doi.org/10.1007/s10973-021-10589-6>
13. Collins IL, Weibel JA, Pan L, Garimella SV (2018) Evaluation of additively manufactured microchannel heat sinks. *IEEE Transactions on Components, Packaging Manufact Technol* 9:446–457. <https://doi.org/10.1109/tcpmt.2018.2866972>
14. Xu C, Xu S, Wang Z, Feng D (2021) Experimental investigation of flow and heat transfer characteristics of pulsating flows driven by wave signals in a microchannel heat sink. *Int Commun Heat and Mass Transfer* 125. <https://doi.org/10.1016/j.icheatmasstransfer.2021.105343>
15. Ozguc S, Pan L, Weibel JA (2021) Optimization of permeable membrane microchannel heat sinks for additive manufacturing. *Appl. Thermal Eng.* 198:117490. <https://doi.org/10.1016/j.applthermaleng.2021.117490>
16. Tan H, Wu L, Wang M, Yang Z, Du P (2019) Heat transfer improvement in microchannel heat sink by topology design and optimization for high heat flux chip cooling. *Int. J. Heat and Mass Transfer*. 129:681–689. <https://doi.org/10.1016/j.ijheatmasstransfer.2018.09.092>
17. Ozguc S, Teague TF, Pan L, Weibel JA (2023) Experimental study of topology optimized, additively manufactured microchannel heat sinks designed using a homogenization approach. *Int. J. Heat and Mass Transfer*. 209:124108. <https://doi.org/10.1016/j.ijheatmasstransfer.2023.124108>

18. Kong D, Jung E, Kim Y, Manepalli VV, Rah KJ, Kim HS, Hong Y, Choi HG, Agonafer D, Lee H (2023) An additively manufactured manifold-microchannel heat sink for high-heat flux cooling. *Int J Mech Sci* 248:108228. <https://doi.org/10.1016/j.ijmecsci.2023.108228>
19. Narendran G, Mallikarjuna B, Nagesha BK, Gnanasekaran N (2023) Experimental investigation on additive manufactured single and curved double layered microchannel heat sink with nanofluids. *Heat Mass Transf* 59:1311–1332. <https://doi.org/10.1007/s00231-022-03336-6>
20. Gerhart PM, Gerhart AL, Hochstein JI (2016) *Munson, young and Okiishi's fundamentals of fluid mechanics*. Wiley, Hoboken
21. Moody LF (1944) Friction factors for pipe flow. *Trans Amer Soc Mech Eng* 66:671–678
22. Zhang Y, Zhang J (2017) Finite element simulation and experimental validation of distortion and cracking failure phenomena in direct metal laser sintering fabricated component. *Additive Manufact* 16:49–57. <https://doi.org/10.1016/j.addma.2017.05.002>
23. Sefene EM (2022) State-of-the-art of selective laser melting process: a comprehensive review. *J Manufact Sys* 63:250–274. <https://doi.org/10.1016/j.jmsy.2022.04.002>
24. Sélo RR, Catchpole-Smith S, Maskery I, Ashcroft I, Tuck C (2020) On the thermal conductivity of AlSi10Mg and lattice structures made by laser powder bed fusion. *Additive Manufact*. 34:101214. <https://doi.org/10.1016/j.addma.2020.101214>
25. White FM (2016) *Fluid mechanics, in SI units*. McGraw-Hill Education, Singapore
26. Kundu PK, Cohen IM, Dowling DR (2012) *Fluid mechanics*. Elsevier, London
27. Bergman TL (2011) *Fundamentals of heat and mass transfer*. Wiley, Hoboken
28. Coleman HW, Steele WG (2009) *Experimentation, validation, and uncertainty analysis for engineers*. Wiley, Hoboken
29. Kandlikar S, Garimella S, Li D, Colin S, King MR (2005) *Heat transfer and fluid flow in minichannels and microchannels*. Elsevier, London
30. Tuckerman DB, Pease RF (1981) High-performance heat sinking for VLSI. *IEEE Electron device letters* 2:126–129. <https://doi.org/10.1109/EDL.1981.25367>
31. Wang H, Chen Z, Gao J (2016) Influence of geometric parameters on flow and heat transfer performance of micro-channel heat sinks. *Appl Thermal Eng* 107:870–879. <https://doi.org/10.1016/j.applthermaleng.2016.07.039>
32. Mohammed HA, Gunnasegaran P, Shuaib NH (2011) Numerical simulation of heat transfer enhancement in wavy microchannel heat sink. *Int. Commun. Heat and Mass Transfer*. 38:63–68. <https://doi.org/10.1016/j.icheatmasstransfer.2010.09.012>
33. Abouali O, Baghernezhad N (2010) Numerical investigation of heat transfer enhancement in a microchannel with grooved surfaces. *ASME J Heat Mass Transfer* 132. <https://doi.org/10.1115/1.4000862>
34. Wang ZH, Wang XD, Yan WM, Duan YY, Lee DJ, Xu JL (2011) Multi-parameters optimization for microchannel heat sink using inverse problem method. *Int J Heat and Mass Transfer* 54:2811–2819. <https://doi.org/10.1016/j.ijheatmasstransfer.2011.01.029>
35. Lin L, Chen YY, Zhang XX, Wang XD (2014) Optimization of geometry and flow rate distribution for double-layer microchannel heat sink. *Int J Thermal Sci* 78:158–168. <https://doi.org/10.1016/j.ijthermalsci.2013.12.009>
36. Leng C, Wang XD, Yan WM, Wang TH (2016) Heat transfer enhancement of microchannel heat sink using transcritical carbon dioxide as the coolant. *Energy Convers Manag* 110:154–164. <https://doi.org/10.1016/j.enconman.2015.12.006>
37. Bejan A, Kraus AD (2003) *Heat transfer handbook* (Vol. 1). Wiley, London
38. Montgomery DC (2017) *Design and analysis of experiments*. Wiley, London

**Publisher's Note** Springer Nature remains neutral with regard to jurisdictional claims in published maps and institutional affiliations.

Springer Nature or its licensor (e.g. a society or other partner) holds exclusive rights to this article under a publishing agreement with the author(s) or other rightsholder(s); author self-archiving of the accepted manuscript version of this article is solely governed by the terms of such publishing agreement and applicable law.